

# EXPERIMENTAL INVESTIGATION OF THE TRANSITION BETWEEN REGULAR AND MACH REFLECTIONS OF A SHOCK WAVE IMPINGING ON A TURBULENT BOUNDARY LAYER

Sven Scharnowski, Rio Baidya, Christian J. Kähler  
Institute of Fluid Mechanics and Aerodynamics  
University of the Bundeswehr Munich  
Werner-Heisenberg-Weg 39, 85577 Neubiberg, Germany  
sven.scharnowski@unibw.de

## ABSTRACT

This work investigates experimentally the interaction of a shock wave generated by means of a  $16^\circ$  wedge with a turbulent boundary layer at a free-stream Mach number of  $M_\infty = 2.56$ . For these flow conditions, an unsteady dual state solution is observed where the shock changes between a regular reflection and a Mach reflection, in contrast to what is predicted by theory. This affects the boundary layer's response and causes large variations of the size and location of the separated flow region below the shock system. The focus of this work is to examine why these types of reflection occur and which phenomena lead to the transition between them. A detailed analysis of velocity fields acquired by means of planar high repetition rate particle image velocimetry allows for the determination of the shock locations and flow direction in the region surrounding the shock interaction. The analysis shows that regular reflection rarely occurs and that Mach reflection with varying Mach stem height is present for about 85% of the measurement time. There is a significant interaction between the partially separated boundary layer flow and the flow field above. Our analysis shows that the transition from Mach reflection to regular reflection is connected to a temporary thickening of the boundary layer upstream of the shock interaction. This phenomenon results in compression waves that alter the Mach number and deflection angle in the region upstream of the shock system, enabling a momentary transition to a regular reflection.

## SHOCK REFLECTION

When a supersonic flow approaches a wedge, a compression shock emanating from the leading edge of the wedge is formed, over which the flow is deflected by the wedge angle. The variables of the flow change abruptly across a shock, whose location is determined by the Mach number of the flow and the deflection caused by the wedge. Pressure, temperature and density increase abruptly and the velocity component perpendicular to the shock front is decelerated to subsonic.

When an oblique shock wave interacts with a turbulent boundary layer, a complex interaction is established. Due to the sudden increase in pressure across the impinging shock and the fact that the pressure of the boundary layer edge equals the wall pressure, the flow tends to detach, resulting in a significant increase in boundary layer thickness. Downstream of the shock interaction the flow attaches again and the boundary layer recovers, as shown in Fig. 1. This results first in com-

pression, then in expansion, and finally in compression again. The resulting shock waves and expansion waves interact with the impinging shock, as discussed in detail by Déleroy and Dussauge (2009) for instance. The incoming shock is indicated as  $C_1$ . Due to the thickening of the boundary layer caused by the increase in pressure over  $C_1$ , the flow upstream of the impingement location of  $C_1$  is deflected away from the wall. This results in a compression that turns into  $C_2$ , the separation shock, which abruptly deflects the incoming flow near the wall upwards.

Depending on which deflections the flow experiences via the shocks  $C_1$  and  $C_2$ , there are two ways in which these shocks may interact. For sufficiently weak deflection angles (whose magnitude depends on the Mach number of the incoming flow) over  $C_1$  and  $C_2$ , the Mach number after these shocks is large enough to allow further deflections over the shocks  $C_3$  and  $C_4$ , such that the direction of flow after the latter shocks is the same on both sides of the slip line. This is a so-called regular reflection, as shown at the left part of Fig. 1. In order for the flow direction after the shocks  $C_3$  and  $C_4$  to be equal, it is necessary for the pressure in these two regions to be identical. However, the shape of the boundary layer thickness also determines the flow direction near the wall. Thus, the location of the shock system and the pressure downstream of the shocks are coupled to the boundary layer edge, as discussed in Déleroy and Dussauge (2009). A contact discontinuity generally emanates from the intersection of the shocks (dashed line in the lower left part of Fig. 1), across which the pressure is the same but the other flow variables may differ.

If the deflections over the shocks  $C_1$  and  $C_2$  become larger, another shock is required in order to enable a continuous transition of pressure and flow direction downstream of the shock system. This shock is a strong solution for the incoming Mach number, which leads to a subsonic flow. Instead of a point-like interaction, two triple points are established between which the shock  $C_M$  is formed, as can be seen in the right part of Fig. 1. Downstream of  $C_M$ , also known as the Mach disk or Mach stem, a subsonic region can be observed that is confined by contact discontinuities emanating from the two triple points. Since the upper contact discontinuity is always steeper than the lower one, the subsonic region becomes tighter and a supersonic flow forms again at some distance from the shock system. This type of reflection is called Mach reflection, which according to Ben-Dor (2006) is a sub-type of irregular shock reflection.

For certain combinations of Mach number and deflection

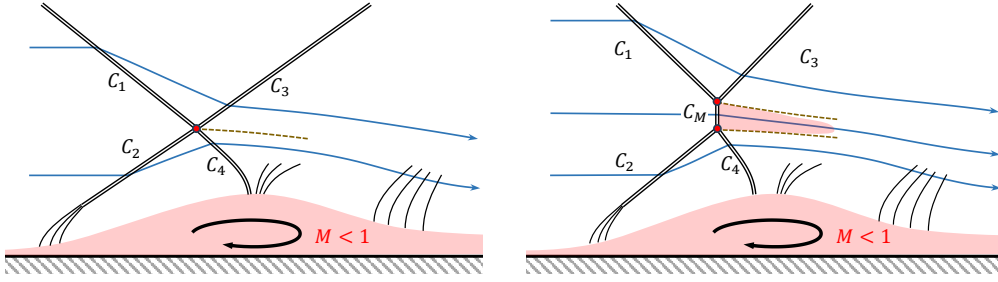


Figure 1. Schematic for the shock-wave boundary layer interaction in case of a regular reflection (left) and a Mach reflection (right).

angle, both Mach reflection and regular reflection can occur. The so-called dual solution domain, where both solutions can theoretically occur, exists only for Mach numbers greater than 2.202 (for perfect gas with a heat ratio of  $\gamma = 1.4$ ) and is initially limited to a small range of flow deflection angles that increases with Mach number (Matheis and Hickel 2015; Xue et al. 2020). Whether Mach reflection or regular reflection occurs depends not only on the Mach number of the inflow and the deflection angle. Other factors that influence the occurrence of Mach reflection are the presence of side walls and the aspect ratio. Mach reflections occur at smaller wedge angles than predicted by two-dimensional theory due to the confinement of the side walls, as shown in experiments and numerical simulations (Bermejo-Moreno et al. 2014; Wang et al. 2015). In addition, the back pressure behind the shock wave boundary layer interaction can cause detachment at the shock generator, thus increasing the deflection angle and changing the reflection type, as discussed in Xue et al. (2020) and Wang et al. (2018). Furthermore, large-scale turbulent structures within the boundary layer locally change the flow direction and thus influence the strength of the separation shock  $C_2$ . This effect can possibly change the reflection type as shown by Matheis and Hickel (2015) by means of numerical flow simulations.

This work presents an experiment in which the vertical distance of the shock generator above a wall is of the same order of magnitude as the width of the test section. With an aspect ratio of 1.16 (width to distance), significant 3D effects occur which lead to irregular reflection instead of the regular reflection expected from 2D theory. The occurring shock waves interact with the turbulent boundary layer flow and show strong variations in their position which occasionally lead to a regular reflection. The objective of the research activity is to characterize the flow fields for both types of reflection, as well as for the transition phases, in detail. This analysis aims to explain how both types of reflection can occur under the same flow conditions and which phenomena lead to the change between the types.

After this introduction, a detailed description of the experimental setup is given and afterwards the main results, including instantaneous velocity field measurements and statistical analyses are outlined. Results are summarized and conclusions are drawn in the last section of this work.

## MEASUREMENT SETUP AND METHODOLOGY

Flow field measurements using particle image velocimetry (PIV) were performed in the trisonic wind tunnel Munich (TWM). For an inflow Mach number of  $M_\infty = 2.56$ , a shock wave was generated by means of a  $16^\circ$  wedge placed in the freestream above a 1.70m long flat plate model, which was mounted at the center of the 300mm wide and 675 mm high

test section. The horizontal wind tunnel walls have a slight divergence of  $\pm 0.4^\circ$ , which compensates for the growing displacement thickness of the wall boundary layers. Two wedge-shaped supports were used to mount the shock generator outside the wall boundary layer at a distance of approximately 75 mm from the upper wall. The wedge angle of  $16^\circ$  is the angle between the model surface and the shock generator. For the shock generator, the leading edge was 257 mm ( $\approx 19\delta_{99}$ ) above the top of the flat plate and its length in streamwise direction is 155 mm ( $\approx 11.5\delta_{99}$ ). Along the flat plate model, a well characterized zero pressure gradient turbulent boundary layer flow develops (Bross et al. 2021), onto which the compression shock impinges about 1.2m downstream of the sharp leading edge. The stagnation pressure and the stagnation temperature of the incoming flow were  $p_0 = 4.0$  bar and  $T_0 = 285$  K, respectively. This leads to a free stream velocity of  $u_\infty = 570$  m/s and a Reynolds number based on the thickness of the undisturbed boundary layer at the impingement location ( $\delta_{99} = 13.5$  mm) of  $Re_{\delta_{99}} = 5.75 \times 10^5$ . Further details about the test facility are provided in Scharnowski et al. (2019).

The flow was seeded with di-ethyl-hexyl sebacate (DEHS) tracer particles which have an average diameter of less than  $1 \mu\text{m}$ . With a response time of approximately  $2 \mu\text{s}$  (Melling 1997; Ragni et al. 2011), the particles can adequately follow the flow for most of the field of view. Only for a small region downstream of the shock is the flow velocity overestimated due to the inertia of the droplets in the region with strong negative acceleration. Velocity field measurements via particle image velocimetry (PIV) were performed in the wall-normal streamwise center plane above the model. The tracers were illuminated from downstream with a light sheet generated by a PIV double pulse laser (DM 150-532, by Photonics Industries Inc.) with a light sheet width of about 0.5 mm. A high speed camera (Phantom V2640, by Vision Research Inc.) equipped with a 35 mm lens (Distagon T\* 35mm f/2, by Zeiss) acquired PIV double images,  $1792 \times 704$  pixel in size (corresponding to  $245 \times 95 \text{ mm}^2$ ), at a recording frequency of 10kHz. The measurement setup with the field of view is sketched in Fig. 2. A total number of 39,000 image pairs were acquired and analysed, which corresponds to  $1.6 \times 10^5$  flow through times, based on  $u_\infty$  and  $\delta_{99}$ . The number of samples is therefore considered to be well suited for statistical analyses.

The PIV measurement setup was optimized to provide an overview of the flow field to determine the position of the shocks, large scale turbulent structures within the boundary layer, and regions with separated flow. Due to the large spatial and temporal dynamics in this type of flow, the resolution of the small-scale features is only partially possible due to the strong velocity gradients in the shear layers, as discussed in Scharnowski and Kähler (2020). In order to enable a reliable evaluation of the PIV data the particle image displacement was

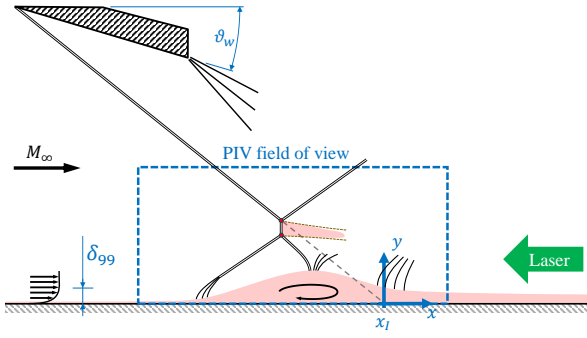


Figure 2. Schematic representation of the experimental setup for the shock wave boundary layer interaction experiments at the TWM. The size and position of the shock generator and the shock system as well as the boundary layer thickness are shown to scale.

limited to 12 pixel for the free stream by setting the time separation between the image pairs to  $3 \mu\text{s}$ . An iterative approach with decreasing interrogation window size and subsequent image deformation was used for the PIV image evaluation. A Gaussian window weighting function was applied and a final interrogation window size of  $12^2$  pixel with 50% overlap was achieved, leading to a vector grid spacing of 0.82 mm corresponding to 5.9% of  $\delta_{99}$  of the undisturbed boundary layer.

## RESULTS AND DISCUSSION

The computed velocity fields were analyzed to identify and evaluate the characteristic features of the different states and the transition between the states. In this section, a characteristic sequence of instantaneous flow fields is discussed in order to describe the temporal evolution of the shock system. The calculated velocity fields show that the two types of reflections from Fig. 1 occur alternately and the state transition is relatively slow. In Fig. 3 a short sequence of exemplary flow fields is presented. Between each of the successive time steps, 13 additional PIV flow fields were recorded, which are not shown here. The time  $t$  at which the flow fields were acquired is normalized by the thickness of the undisturbed boundary layer and the velocity of the free-stream  $\tau = t \cdot u_\infty / \delta_{99}$ . For the time steps in Fig. 3 the time is shifted such that the case of regular reflection is at  $\tau' = 0$ . From the PIV velocity fields the location of the shocks were identified from the strongest gradients  $\partial u / \partial x$  and  $\partial v / \partial x$  and are indicated by dashed lines in the instantaneous flow fields of the figure. The shock wave  $C_1$  originating from the wedge deflects the incoming flow downwards. In response to the impinging shock, the boundary layer thickness starts to increase from about  $(x - x_1) / \delta_{99} = -10$ . The suddenly growing boundary layer thickness leads to a compression of the flow, which transitions into the shock  $C_2$ , over which the flow directly above the boundary layer is deflected upwards, indicated by red color in Fig. 3. The shock waves  $C_1$  and  $C_2$  intersect, resulting in either a regular intersection (bottom row in Fig. 3) or a Mach stem with two triple points (top row in Fig. 3).

In the case of the regular reflection, it is noticeable that the flow direction upstream of the shock system is slightly upward, i.e. the angle of the flow direction  $\vartheta$  is greater than zero. The region with upward flow direction is initially limited to the section directly in front of the shock  $C_2$ , then becomes larger until it occupies about  $4 \delta_{99}$  in the horizontal direction. The reason of this change in flow direction is a compression caused

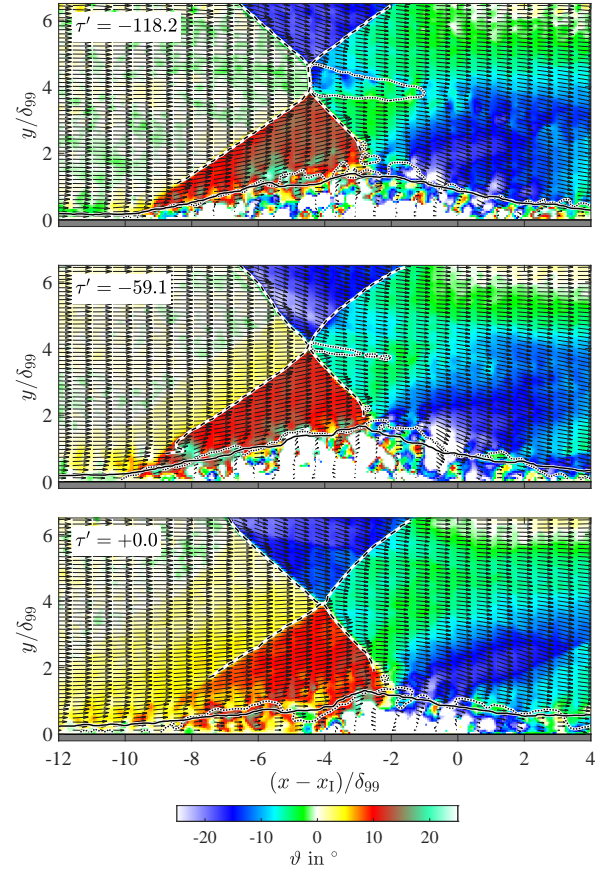


Figure 3. Instantaneous velocity fields showing the transition from Mach reflection (top) to regular reflection (bottom). The background color represents the flow direction  $\vartheta$ . The shock location, the sonic line, and the boundary layer displacement thickness are indicated by dashed, dotted, and solid lines, respectively.

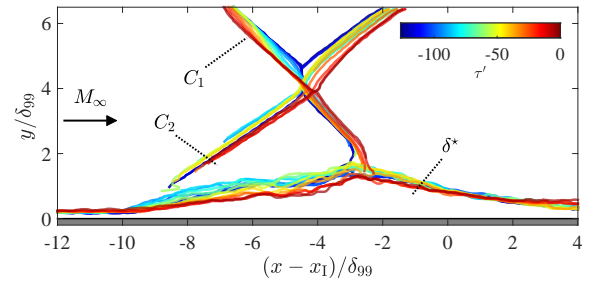


Figure 4. Superimposed visualization of the temporal development of the shock location and displacement thickness during transition from Mach reflection to regular reflection covering the same time span as in Fig. 3. The line color indicate the elapsed time.

by an increase in the displacement thickness of the boundary layer in the region between  $(x - x_1) / \delta_{99} = -12$  and  $-8$ .

In order to better recognize the changes in the position of the shocks and the boundary layer, Fig. 4 shows the temporal evolution of the detected shock system covering the same time span as in Fig. 3. Starting from a Mach reflection at  $\tau' = -118.2$  ms (blue color in Fig. 4), two oblique shocks  $C_1$  and  $C_2$  as well as a normal shock occur. The values for

the deflection angle across the shocks  $C_1$  and  $C_2$  are approximately  $-19^\circ$  and  $+14^\circ$ , leading to Mach numbers of 1.75 and 1.96, respectively. The deflection across shock  $C_1$  exceeds the wedge angle of the shock generator. This may be due to the influence of the sidewalls, as previously noted by Bermejo-Moreno et al. (2014) and Wang et al. (2015). The deflection over shock  $C_2$  falls within the range reported by Matheis and Hickel (2015) for Mach numbers of 2.0 and 3.0. Downstream of the shock  $C_1$ , the flow is redirected again across the shock  $C_3$ . The resulting flow direction near the upper triple point is around  $-10^\circ$  and shifts further away from the triple point to values around  $-5^\circ$ . Downstream of the shock  $C_2$ , the flow is redirected again by the shock  $C_4$ , resulting in a flow direction of  $-6^\circ$  near the lower triple point, which is reduced to values around  $-3^\circ$  further away from the triple point. Between the two triple points, the flow is slowed down by a single shock, the Mach stem  $C_M$ . This is a strong shock that deflects the flow slightly towards the wall and reduces the Mach number to values around 0.52.

In the case of regular reflection at  $\tau' = 0$  (red color in Fig. 4), the Mach number before  $C_2$  is decreased to 2.3 and the flow direction is slightly upwards (around  $+3^\circ$ ). This is caused by weak compression waves emanating from the boundary layer upstream of the shock system, as visible, in the bottom row of Fig. 3. The position of the incoming shock  $C_1$  is temporarily shifted slightly towards the wall because of the interaction with the compression waves. The shock  $C_2$  is also shifted towards the wall, as the boundary layer below the shock is now slightly thinner. The shocks  $C_1$  and  $C_2$  meet approximately at the same height as the lower triple point from the Mach reflection and slightly downstream of it.

The change in flow direction across the shock  $C_1$  is smaller for the regular reflection for the lower part of the shock and is around  $-13.5^\circ$ . The deflection via  $C_2$  is also smaller (approx.  $+10^\circ$ ) compared to the Mach reflection. The shocks  $C_3$  and  $C_4$  deflect the flow such that it has the same flow direction of about  $-7^\circ$  in the region after the interaction. This flow angle is significantly steeper than the one reported by Matheis and Hickel (2015) for numerical simulations at Mach numbers of 2.0 and 3.0. In the experiment shown here, the boundary layer thickness recovers faster downstream of the shock interaction. The flow direction after the shock interaction and the shock strength are coupled and both determine the resulting flow field with the position of the shocks and the type of reflection.

The boundary layer's displacement thickness  $\delta^*$  below the shock interaction is decreased during regular reflection. Furthermore,  $\delta^*$  is slightly thicker upstream ( $(x - x_1)/\delta_{99} < -10$  and downstream  $(x - x_1)/\delta_{99} > 2$  of the interaction region for the red line, which corresponds to a regular reflection, as can be seen in Fig. 4. The displacement thickness therefore grows slower in the case of regular reflection, which also results in less deflection of the flow.

For the combination of Mach number and wedge angle investigated here, Mach reflection can be observed for most of the time, whereby the distance between the triple points and thus also the subsonic region downstream of the shock interaction varies strongly. Only rarely does the position of the triple points coincide and there is a transition to regular reflection. However, this state is obviously not stable and therefore only maintained for a few milliseconds before the Mach reflection is established again.

The temporal development of the Mach number along horizontal and vertical lines is shown in Figs. 5 and 6, respectively. The local Mach number was estimated from the local

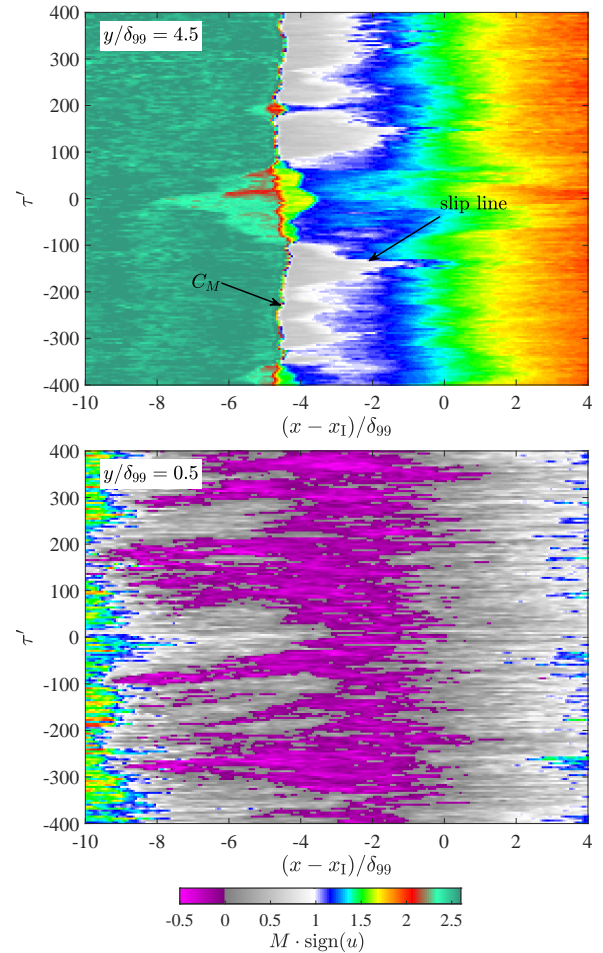


Figure 5. Temporal development of the Mach number along a horizontal line at  $y/\delta_{99} = 4.5$  and  $0.5$ . At the time  $\tau' = 0$  the shock reflection type has changed from Mach reflection to a regular reflection.

velocity's absolute value  $U$  as follows:  $M = U/\sqrt{\gamma RT}$ . Where the local temperature  $T$  is computed using the energy equation  $T = T_0 - U^2(\gamma - 1)/(2\gamma R)$ . Here  $\gamma$  is the specific heat ratio,  $R$  is the gas constant, and  $T_0$  is the total temperature measured in the settling chamber of the wind tunnel.

In Fig. 5 the data for a height of  $y/\delta_{99} = 4.5$ , i.e. through the shock  $C_M$  as well as close to the wall at  $y/\delta_{99} = 0.5$  are shown over a time span of  $\tau' = 800$ . In the top row of Fig. 5, the subsonic region downstream of the shock  $C_M$  is clearly visible. The slip line that bounds the subsonic region is characterized by strong fluctuations, as the subsonic region moves in the vertical direction and also changes its size, as already seen in Fig. 3. In the case of regular reflection, i.e. around  $\tau' = 0$ , the subsonic region disappears completely and the plane intersects shocks  $C_1$  and  $C_3$ .

Near the wall at  $y/\delta_{99} = 0.5$  there is subsonic flow in almost the entire field of view. Supersonic flow only exists for  $(x - x_1)/\delta_{99} < -9$  and  $> 3$ . Flow separation occurs in this subsonic region. The size of the separated flow region varies greatly within the time range shown. The beginning of the region appears to vary considerably more than the downstream end.

Figure 6 shows the Mach number along a vertical line upstream and downstream of the shock interaction as a function of time. The position of the shock  $C_1$  is relatively stable, but

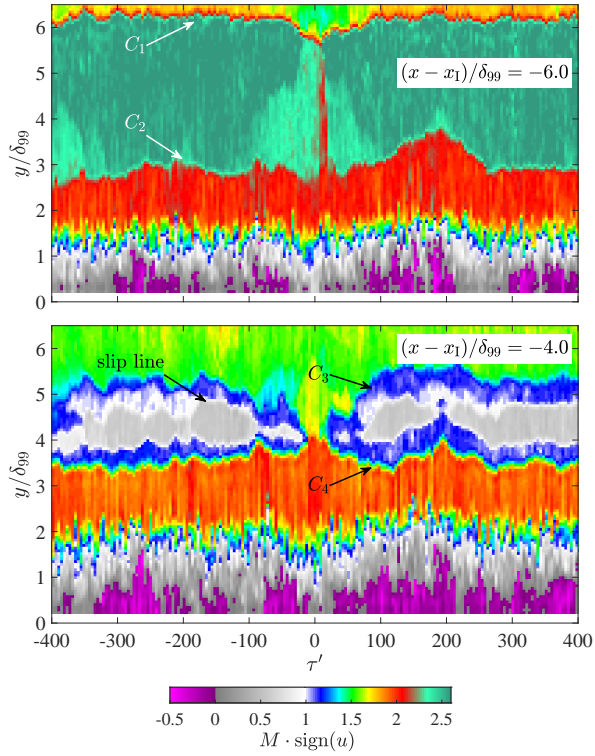


Figure 6. Temporal development of the Mach number along vertical lines before the shock interaction at  $(x - x_1)/\delta_{99} = -6.0$  (top) and downstream of it at  $(x - x_1)/\delta_{99} = -4.0$  (bottom). At the time  $\tau' = 0$  the shock reflection type has changed from Mach reflection to a regular reflection.

the other shocks show strong variations in their height. In particular,  $C_3$  moves significantly during the transition to the regular reflection, as shown in the lower part of Fig. 6. During the regular reflection, the shock  $C_1$  is shifted downwards due to the compression emanating from the boundary layer and  $C_2$  becomes weaker and finally disappears almost completely for  $\tau' = 0$ , as can be seen in the upper part of Fig. 6. Downstream of the shock interaction there are two contact discontinuities, between which there is a subsonic region. The vertical extent of the subsonic region and thus Mach stem height and the distance between the triple points is subject to strong variations, with maximum values in the order of  $\delta_{99}$  being reached. In Matheis and Hickel (2015), a similar height of the Mach stem was reported for a Mach number of 2.0. However, for the case of  $M_\infty = 3.0$ , which has a reduced boundary layer thickness by a factor of about four, the relative Mach stem height was significantly larger. During regular reflection, both discontinuities merge and there is no subsonic zone (bottom row in Fig. 6). This means that there is a significant difference in the loss of momentum downstream of the shocks for the two types of shock reflection. It is therefore important to be able to predict when there will be a change in the type of reflection.

Beneath the shock interaction, flow separation repeatedly occurs both at  $(x - x_1)/\delta_{99} = -6.0$  and at  $-4.0$  as can be seen from the negative flow velocity in Fig. 6. The strength of the separation does not appear to correlate directly with the type of reflection. However, it is noticeable that in the case of regular reflection, almost no back-flow occurs at either position.

The separated flow region below the shock interaction exhibits significant fluctuations in size, as depicted in the bottom line of Fig. 5. Looking at the probability distribution for

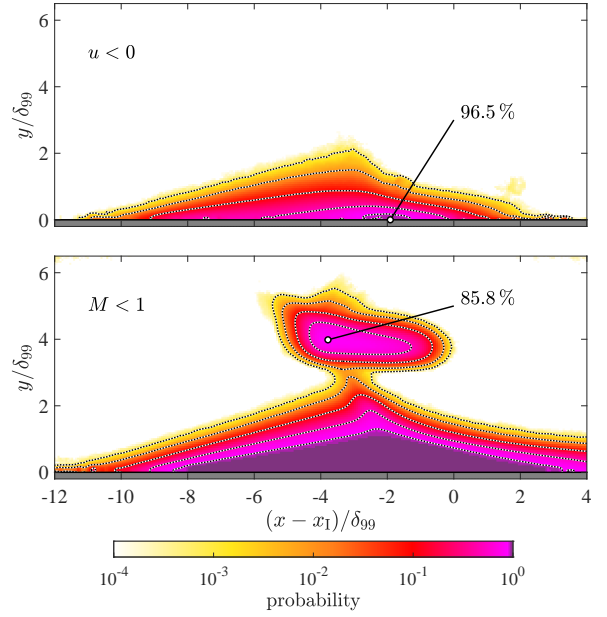


Figure 7. Spatial distribution of the separated flow probability (top) and the subsonic flow probability (bottom) with contour lines at levels of 0.1, 1.0, 10, 50 and 90%.

separated flow in the upper part of Fig. 7, it can be seen that separated flow occurs at least occasionally in the entire region between  $(x - x_1)/\delta_{99} = -11$  and  $+3$ . At  $(x - x_1)/\delta_{99} = -2.0$ , the probability of encountering separated flow near the wall peaks at 96.5%. In contrast to pure regular reflection at lower Mach numbers, as seen in Baidya et al. (2020) and Humble et al. (2009), where detachment only occurred for individual time steps but not on average, the separated flow occurs much more frequently. Given the higher pressure increase associated with a Mach reflection, this result was expected.

In the lower part of Fig. 7, the probability distribution of encountering subsonic flow is shown. The shape of the subsonic region near the wall reflects the development of the boundary layer. The presence of subsonic flow downstream of the shock interaction indicates Mach reflection. Since there is a local maximum of 85.6% in this region, regular reflection occurs in about 14.4% of the data.

The auto-correlation of the velocity signal is used to determine which characteristic time scales are present in both reflection types. Figure 8 shows the width of the peak of the auto-correlation function of the horizontal velocity component for each measurement point in the field of view. For the region upstream of the shock system, at some distance downstream of it as well as downstream of the shocks  $C_2$  and  $C_4$ , the correlation length is so short that successive velocity fields with a temporal separation of  $\Delta\tau = 4.2$  do not correlate with each other. In contrast to this, a correlation time of the order of  $\Delta\tau = 100$  is achieved in the area of the shocks and even higher values of up to  $\Delta\tau = 370$  are reached for the shock interaction region and between the shocks  $C_1$  and  $C_3$ .

With a correlation time in the order of  $\tau = 100$ , the transition between the reflection types is a relatively slow process. Comparable frequencies corresponding to this time scale have also been found for the expansion-contraction cycle of separation bubbles in shock-wave boundary layer interactions for a compression–expansion ramp configuration (Grilli et al. 2012) as well as in a shock reflection configuration (Piponniau et al. 2009).

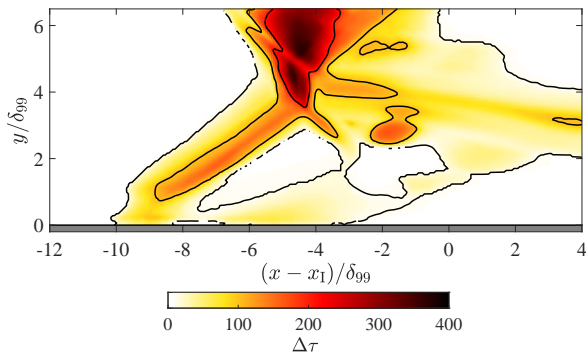


Figure 8. Spatial distribution of the width of the auto-correlation function of the horizontal velocity component at half the height of the correlation maximum. Contour lines are shown for  $\Delta\tau = 10, 100,$  and  $200$ .

### Summary and conclusions

In this work, a shock wave generated at a  $16^\circ$  wedge and interacting with a turbulent boundary layer flow at Mach number 2.56 has been considered with the aim to characterize the two occurring reflection types and their transition. According to the theory for two-dimensional stationary flow, the angle of the incoming shock (although increased by 3D effects) and that of the detachment shock lead to a regular reflection. However, in contrast to theory a Mach reflection occurs for about 85% of the observed time steps. This can be explained by the flow angle that occurs after the shock interaction. A regular reflection requires a flow angle downstream of the shock interaction which is less steep than compared to the one observed in the experiment.

The incoming shock leads to a thickening of the boundary layer accompanied by a flow separation on the average as well as in the individual flow fields. Only if the boundary layer displacement thickness upstream of the shock  $C_2$  increases to an above-average level, the flow is compressed and deflected upwards, resulting in a reduction of the Mach number and a change to a regular reflection. However, the compression in front of the shock system is not stable and the reflection type switches back to Mach reflection. On average, the duration of a regular reflection is of the order of about 100 flow through times.

### ACKNOWLEDGEMENTS

Funding for this work was provided by the German Research Foundation (Deutsche Forschungsgemeinschaft) through research grants (project no. 448354709), which is gratefully acknowledged.

### References

Baidya, R., S. Scharnowski, M. Bross, and C. J. Kähler (2020). “Interactions between a shock and turbulent features in a Mach 2 compressible boundary layer”. In: *Journal of Fluid Mechanics* 893, A15. DOI: [10.1017/jfm.2020.208](https://doi.org/10.1017/jfm.2020.208).

Ben-Dor, G. (2006). “A state-of-the-knowledge review on pseudo-steady shock-wave reflections and their transition criteria”. In: *Shock Waves* 15.3, pp. 277–294. DOI: [10.1007/s00193-006-0036-z](https://doi.org/10.1007/s00193-006-0036-z).

Bermejo-Moreno, I., L. Campo, J. Larsson, J. Bodart, D. Helmer, and J. K. Eaton (2014). “Confinement effects in shock wave/turbulent boundary layer interactions through wall-modelled large-eddy simulations”. In: *Journal of Fluid Mechanics* 758, 562. DOI: [10.1017/jfm.2014.505](https://doi.org/10.1017/jfm.2014.505).

Bross, M., S. Scharnowski, and C. J. Kähler (2021). “Large-scale coherent structures in compressible turbulent boundary layers”. In: *Journal of Fluid Mechanics* 911, A2. DOI: [10.1017/jfm.2020.993](https://doi.org/10.1017/jfm.2020.993).

Délery, J. and J.-P. Dussauge (Dec. 2009). “Some physical aspects of shock wave/boundary layer interactions”. In: *Shock Waves* 19.6, pp. 453–468. ISSN: 1432-2153. DOI: [10.1007/s00193-009-0220-z](https://doi.org/10.1007/s00193-009-0220-z).

Grilli, M., P. J. Schmid, S. Hickel, and N. A. Adams (2012). “Analysis of unsteady behaviour in shockwave turbulent boundary layer interaction”. In: *Journal of Fluid Mechanics* 700, pp. 16–28. DOI: [10.1017/jfm.2012.37](https://doi.org/10.1017/jfm.2012.37).

Humble, R. A., F. Scarano, and B. W. Van Oudheusden (2009). “Unsteady aspects of an incident shock wave/turbulent boundary layer interaction”. In: *Journal of Fluid Mechanics* 635, pp. 47–74. DOI: [10.1017/S0022112009007630](https://doi.org/10.1017/S0022112009007630).

Matheis, J. and S. Hickel (2015). “On the transition between regular and irregular shock patterns of shock-wave/boundary-layer interactions”. In: *Journal of Fluid Mechanics* 776, 200234. DOI: [10.1017/jfm.2015.319](https://doi.org/10.1017/jfm.2015.319).

Melling, A. (1997). “Tracer particles and seeding for particle image velocimetry”. In: *Meas Sci Technol* 8, pp. 1406–1416. DOI: [10.1088/0957-0233/8/12/005](https://doi.org/10.1088/0957-0233/8/12/005).

Piponniau, S., J.-P. Dussauge, J.-F. Debieve, and P. Dupont (2009). “A simple model for low-frequency unsteadiness in shock-induced separation”. In: *Journal of Fluid Mechanics* 629, pp. 87–108. DOI: [10.1017/S0022112009006417](https://doi.org/10.1017/S0022112009006417).

Ragni, D., F. Schrijer, B. W. Van Oudheusden, and F. Scarano (2011). “Particle tracer response across shocks measured by PIV”. In: *Experiments in Fluids* 50.1, pp. 53–64. DOI: [10.1007/s00348-010-0892-2](https://doi.org/10.1007/s00348-010-0892-2).

Scharnowski, S., M. Bross, and C. J. Kähler (2019). “Accurate turbulence level estimations using PIV/PTV”. In: *Experiments in Fluids* 60.1, p. 1. ISSN: 1432-1114. DOI: [10.1007/s00348-018-2646-5](https://doi.org/10.1007/s00348-018-2646-5).

Scharnowski, S. and C. J. Kähler (2020). “Particle Image Velocimetry – classical operating rules from today’s perspective”. In: *Optics and Lasers in Engineering*, p. 106185. DOI: <https://doi.org/10.1016/j.optlaseng.2020.106185>.

Wang, B., N. D. Sandham, Z. Hu, and W. Liu (2015). “Numerical study of oblique shock-wave/boundary-layer interaction considering sidewall effects”. In: *Journal of Fluid Mechanics* 767, 526561. DOI: [10.1017/jfm.2015.58](https://doi.org/10.1017/jfm.2015.58).

Wang, C., L. Xue, and K. Cheng (2018). “Application of the minimum entropy production principle to shock reflection induced by separation”. In: *Journal of Fluid Mechanics* 857, 784805. DOI: [10.1017/jfm.2018.762](https://doi.org/10.1017/jfm.2018.762).

Xue, L., F. F. J. Schrijer, B. W. van Oudheusden, C. Wang, Z. Shi, and K. Cheng (2020). “Theoretical study on regular reflection of shock waveboundary layer interactions”. In: *Journal of Fluid Mechanics* 899, A30. DOI: [10.1017/jfm.2020.455](https://doi.org/10.1017/jfm.2020.455).